European Rotorcraft Forum

DYNAMICS AND STABILITY ISSUES OF A SYNCH-ROTOR AIRCRAFT

Giulio Avanzini, giulio.avanzini@unisalento.it, University of Salento (Italy)

Giulia Bertolani, giulia.bertolani2@unibo.it, University of Bologna (Italy)

Emanuele Luigi de Angelis, emanuele.deangelis4@unibo.it, University of Bologna (Italy)

Fabrizio Giulietti, fabrizio.giulietti@unibo.it, University of Bologna (Italy)

Gianluca Rossetti, gianluca.rossetti3@unibo.it, University of Bologna (Italy)

Abstract

This paper presents an analytical framework for addressing the stability analysis of a synch-rotor configuration. By linearization about some different trim conditions, a linearized model is obtained made by the decoupled longitudinal and lateral/directional dynamics. A detailed analysis of the stability derivatives and natural modes is given, showing how relevant design parameters, proper of the intermeshing rotors configuration, affect the rotorcraft dynamical behavior. A numerical test case is discussed in support of the proposed model.

1. INTRODUCTION

In the last decade Remotely–Piloted Aerial Systems (RPAS), particularly small battery–powered fixed and rotary–wing platforms, gained a large interest in the scientific and industrial community. Reduced size, weight, and operational costs together with the large availability of low-cost avionics make such systems a suitable solution for a wide range of applications, including load transportation, search and rescue, and remote sensing. In this scenario, rotary wing configurations (helicopters and multi-rotor aircraft) showed to be particularly attractive. As a matter of fact, vertical take-off and landing and hovering capabilities largely increase the effectiveness of their operations, especially in restricted and obstructed areas. A particular rotary-wing aircraft configuration is represented by the synch-rotor, where the total thrust is provided by two counter-rotating intermeshing main rotors, allowing at the same time for the yaw-axis torque balance. Existing literature of such configuration is mainly related to the Kaman K-MAX® aircraft, where performance, vibratory loads analysis, servo-flaps design, identification and control system design have been addressed [1] [2] [3] [4] whereas other works are related to system identification of small-scale platform projects [5] [6]. In the recent past, synch-rotor configuration started becoming attractive among rotary-wing unmanned platform. With respect to the coaxial helicopter configuration, the larger 'free' disc area of the inter-meshing rotor configuration increases the lifting capability leading to a 10-15 percent larger available payload, due to the reduced interference effects [6]. The noise level of the inter-meshing configuration is also reduced and the lack of manoeuvrability with respect to the coaxial helicopter can be partially recovered by means of a proper control system design.

Although all the above mentioned studies to synch-rotor aircraft cover a wide range of topics related to such configuration, to the best of the authors' knowledge, most of the current research focuses on performances analysis based on experimental validation without providing a generalized theoretical framework for addressing preliminary design, optimal sizing and control system design. Moreover, the few existing models are obtained from Kaman K-MAX® (and other small unmanned platforms) by means of systems identification algorithms. Thus, an analytical framework aimed at accurately describing aircraft performance, dynamics behaviour and stability issues as a result of relevant configuration parameters is still missing in the literature.

The scope of the present paper is to present an extension of a previous work done by some of the authors [7] with the aim to fill this gap by presenting analytical framework where the rotors thrust and the natural dynamics of an unmanned synch-rotor are derived as a function of configuration parameters. The design process of this configuration is a challenging task: on one side, the absence of a tail rotor drives this configuration to an exceptional high ratio of lift per horsepower and a very stable hovering performance. On the other side, two overlapping rotors allow for a more compact design (with respect a single main rotor of the same area) while affecting the overall aerodynamic efficiency. Since performance and stability are closely related to rotors configurations parameters, a proper mathematical model becomes may represent a valuable tool for aircraft preliminary sizing and control system design. In particular, the following three main results are provided:

- a linearized model, made of two decoupled subsystems and some approximate closed-form solutions for relevant dynamic modes;
- a detailed stability analysis showing the relationship between aircraft configuration and dynamics behaviour.

The rest of the paper is structured as follows. Sections 2 and 3 address the nonlinear and linearized models, respectively. In Section 4 stability analysis is presented. A section of concluding remarks ends this paper.

2. MATHEMATICAL MODELLING

The proposed mathematical framework consists of the complete non-linear equations of motions and includes the modelling of forces and moments acting on the vehicle. Geometrical considerations about rotors design are

presented with main rotors equations. The following assumptions are made:

- The earth is flat and fixed;
- Mass, inertia and center of gravity position are constant; accordingly, fuel consumption is neglected and the vehicle presents a longitudinal plane of symmetry;
- Gravity acceleration is considered independent of height and hence constant.

2.1. Reference frames and coordinate transformation

The following reference frames are introduced, as depicted in Figure 1, Figure 2 and Figure 3:

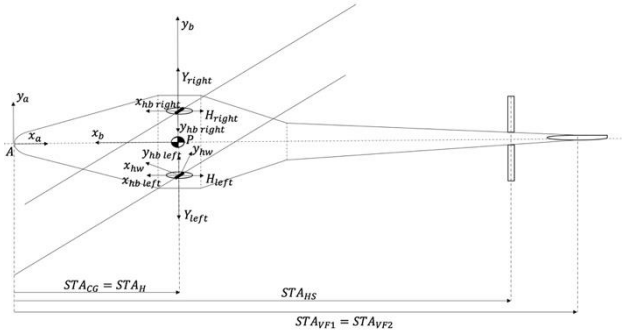

Figure 1: Synch-rotor XY view

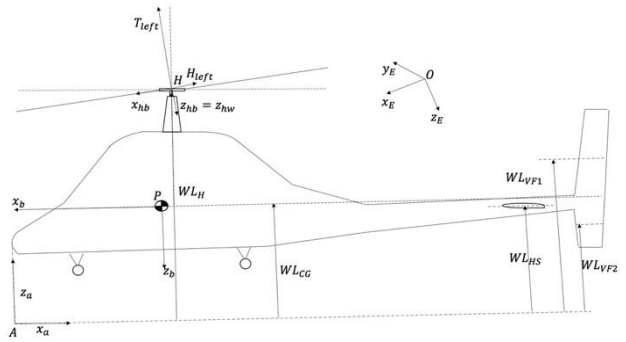

Figure 2: Synch-rotor XZ view

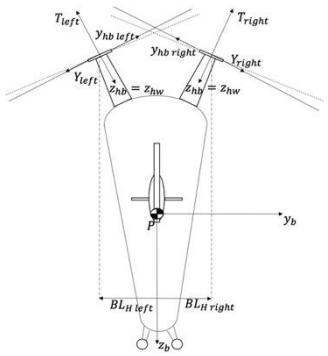

Figure 3: Synch-rotor YZ view

Hub-Wind, Hub-Body, Body, Aircraft, Local Wind and NED. In particular, the term "Hub" means that the origin of the coordinate system is at the hub centre. The terms "Wind" and "Body" indicate where the three axes point.

1. An Earth-fixed North–East-Down frame, $\mathbb{F}_E = \{O;\ \boldsymbol{x}_E, \boldsymbol{y}_E, \boldsymbol{z}_E\}$. This frame is inertial under the assumption of flat and non- rotating Earth.
2. Hub Wind Frame $\mathbb{F}_{hw} = \{H;\ \boldsymbol{x}_{hw}, \boldsymbol{y}_{hw}, \boldsymbol{z}_{hw}\}$. This frame is used in calculation of rotor forces and moments. Its origin is the rotor hub. $\mathbf{z}_{hw}$ axis is aligned with the rotor shaft, pointing upward. $\mathbf{x}_{hw}$ axis (horizontal) is aligned with the component of relative wind normal to the shaft axis. $\mathbf{y}_{hw}$ axis completes the right-handed orthogonal set.
3. Hub Body Frame $\mathbb{F}_{hb} = \{H;\ \boldsymbol{x}_{hb}, \boldsymbol{y}_{hb}, \boldsymbol{z}_{hb}\}$. $\mathbf{z}_{hb}$ axis is aligned with rotor shaft, pointing upward. This system coincides with the hub-wind system when the sideslip β_w is zero.
4. Body Fixed Frame $\mathbb{F}_b = \{P;\ \boldsymbol{x}_b, \boldsymbol{y}_b, \boldsymbol{z}_b\}$. Origin is located at the centre of gravity of the rotorcraft. $\mathbf{x}_b$ axis points in forward direction, it's aligned with the longitudinal axis of the vehicle; $\mathbf{z}_b$ axis points downward and $\mathbf{y}_b$ axis completes the right-hand system. All forces and moments used in the body equations of motion are expressed relative to this system.
5. Aircraft Frame $\mathbb{F}_a = \{A;\ \boldsymbol{x}_a, \boldsymbol{y}_a, \boldsymbol{z}_a\}$. The origin is typically located ahead and below the rotorcraft at some arbitrary point within the plane of symmetry. The reference axes are parallel to the Body axes, but $\mathbf{z}_a$ axis, called Waterline, points upward; $\mathbf{x}_a$ axis, named Stationline, points from bow to stern; $\mathbf{y}_a$ axis, Buttline, is positive to the pilot's right. All forces and moments and centre of gravity are located with these reference axes.
6. A set of Local Wind Frame $\mathbb{F}_{jw} = \{R_j;\ \boldsymbol{x}_{jw}, \boldsymbol{y}_{jw}, \boldsymbol{z}_{jw}\}$. These axes are used to calculate lift and drag forces on empennage and on the fuselage. For each surface, the origin is at the quarter point of the mean aerodynamic chord and the lift is normal to the relative wind and to a spanwise line passing through the quarter chord point.

Rotor flapping dynamics assessment and rotor forces and moments calculation require linear and angular velocity vectors and acceleration vector as expressed in the Hub-Body system and the angle of sideslip at the hub. The cyclic pitch is also requested in Hub-Wind system.
In this respect, the velocity vector at the hub is written as follows:

$$V_h = \Pi_{hb}\left(V_b + \begin{bmatrix} l_{mr} \\ y_{mr} \\ h_{mr} \end{bmatrix} \times \Omega_b\right) \tag{1}$$

whereas angular velocity and acceleration are given by:

$$\boldsymbol{\Omega}_h = \Pi_{hb}\boldsymbol{\Omega}_b \tag{2}$$

$$\dot{\boldsymbol{\Omega}}_h = \Pi_{hb}\dot{\boldsymbol{\Omega}}_b \tag{3}$$

where Π_{hb} is the rotational matrix from Body to Hub-Body system, that is:

(4) $$\Pi_{hb} = \begin{bmatrix} 1 & 0 & 0 \\ 0 & \cos\frac{\Gamma}{2} & -\sin\frac{\Gamma}{2} \\ 0 & \sin\frac{\Gamma}{2} & \cos\frac{\Gamma}{2} \end{bmatrix}$$

Γ is the tilt angle between the rotors masts. In order to implement the calculated Hub-Body components into the 6-DOF equations of motion, these are rotated into the Wind-Hub system:

(5) $$\begin{bmatrix} (\ )_x \\ (\ )_y \\ (\ )_z \end{bmatrix}_{wh} = \begin{bmatrix} \cos\beta_w & \sin\beta_w & 0 \\ -\sin\beta_w & \cos\beta_w & 0 \\ 0 & 0 & 1 \end{bmatrix} \begin{bmatrix} (\ )_x \\ (\ )_y \\ (\ )_z \end{bmatrix}_{hb}$$

where

(6) $$\beta_w = \sin^{-1}\frac{v_h}{(v_h^2 + u_h^2)^{1/2}}$$

is the sideslip angle.

2.2. Equations of motion

Rotorcraft dynamics is described by Newton-Euler equations of motion projected in $\mathbb{F}_b$. Namely:

(7) $$\dot{\mathbf{V}} = -\boldsymbol{\Omega} \times \mathbf{V} + \mathbf{F}^{(e)}/m$$

(8) $$\dot{\boldsymbol{\Omega}} = \mathbf{I}^{-1}[-\boldsymbol{\Omega} \times (\mathbf{I}\boldsymbol{\Omega}) + \mathbf{M}^{(e)}]$$

where mass and mass distribution are assumed to be constant.
Rotorcraft attitude kinematics is given by:

(9) $$\begin{bmatrix} \dot{\phi} \\ \dot{\theta} \\ \dot{\psi} \end{bmatrix} = \begin{bmatrix} 1 & \sin\phi\tan\theta & \cos\phi\tan\theta \\ 0 & \cos\phi & -\sin\phi \\ 0 & \sin\phi / \cos\theta & \cos\phi / \cos\theta \end{bmatrix} \Omega$$

(10) $$\frac{d}{dt}\begin{bmatrix} x \\ y \\ z \end{bmatrix} = R_b^{hb}\begin{bmatrix} u \\ v \\ w \end{bmatrix}$$

provided

(11) $$R_b^{hb} = \begin{bmatrix} c\theta c\psi & s\phi s\theta c\psi - c\phi s\psi & c\phi s\theta c\psi + s\phi s\psi \\ c\theta s\psi & s\phi s\theta s\psi + c\phi c\psi & c\phi s\theta s\psi - s\phi c\psi \\ -s\theta & s\phi c\theta & c\phi c\theta \end{bmatrix}$$

where c stays for cos and s for sin.

2.3. Forces and moments

The external forces are made of aerodynamic forces $\boldsymbol{F}^{(a)}$ and gravity forces $\boldsymbol{F}^{(g)}$ contributions, whereas total moments include aerodynamic moments $\boldsymbol{M}^{(a)}$.
Gravity forces are expressed in the following way:

(12) $$\mathbf{F}^{(g)} = \Pi_{be}\begin{bmatrix} 0 \\ 0 \\ mg \end{bmatrix} = \begin{bmatrix} -mg\sin\theta \\ mg\sin\phi\cos\theta \\ mg\cos\phi\cos\theta \end{bmatrix}$$

Aerodynamic effects are introduced for all rotorcraft components and summed:

(13) $$\mathbf{F}^{(a)} = \mathbf{F}^{(rot.)} + \mathbf{F}^{(fus.)} + \mathbf{F}^{(vert.stab.)} + \mathbf{F}^{(horiz.stab.)}$$

(14) $$\mathbf{M}^{(a)} = \mathbf{M}^{(rot.)} + \mathbf{M}^{(fus.)} + \mathbf{M}^{(vert.stab.)} + \mathbf{M}^{(horiz.stab.)}$$

2.3.1 Main rotors model

The intermeshing rotors system is made of two single-counter-rotating main rotors. For the mathematical modelling purposes, equations for a single counter clockwise rotor are first derived. Then, by means of symmetrical coordinate systems [8], equations for the second rotor are obtained. Interference effects related to the overlapping disc area are then included. Blades are assumed rigid with integral form dependent on control actions, vehicle cinematics and flapping equations. Rotor is assumed as a teetering one. Flapping dynamics is approximated using a tip-path plane representation [9]. The following assumptions are introduced:

1. Rotor blade is rigid in bending and torsion;
2. Linear blade twist;
3. Flapping and inflow angles are assumed small, the analysis is based on a simple strip theory;
4. Only effects due to angular acceleration $\dot{p}$ and $\dot{q}$, angular velocity p, q and the normal acceleration of the aircraft motion are considered to calculate blade flapping;
5. Compressibility and stall effects are not considered;
6. Reversed flow region is not considered;
7. The inflow is assumed to be uniform;
8. The tip loss factor is assumed to be 1;
9. Blade flapping is approximated by the first harmonic terms with time-varying coefficients, that is:

(15) $$\beta(t) = a_0(t) - a_1(t)\cos\psi - b_1(t)\sin\psi$$

The analytical tip-path plane dynamic equations are:

(16) $$\ddot{\bar{\mathbf{a}}} + \tilde{D}\dot{\bar{\mathbf{a}}} + \tilde{K}\bar{\mathbf{a}} = \tilde{\bar{f}}$$

where $\boldsymbol{a} = (a_0 \quad a_1 \quad b_1)^T$ and expressions for $\tilde{D}$, $\tilde{K}$, $\tilde{f}$ terms are reported in Ref. [9]. According to blade flapping approximation in equation (15), a_0 is treated as a preset constant and coefficients $a_1(t)$ and $b_1(t)$ can be solved for by setting $\varepsilon = \dot{a}_0 = \ddot{a}_0 = 0$ in equation (16).
Given the above assumptions, in conjunction with the development of tip-path plane dynamic equations, in forces and moments equations momentum theory is utilized and blade forces are analytically integrated over the radius. Contributions functions of the azimuth of each blade are summed. Detailed expressions for the derivation of forces and moments are given in Ref. [9].
The rotor inflow ratio is required in the computation of thrust. There are two main categories of inflow models: static and dynamic. The Pitt-Peters dynamic inflow model [10] has been used, only considering a uniform inflow. The induced uniform inflow model implemented is assumed to be, in the wind-hub reference frame:

(17) $$\frac{dy}{dx} = \begin{pmatrix} \lambda_0 \\ \lambda_s \\ \lambda_c \end{pmatrix} = \Omega\mathbb{M}^{-1}\left(-(\mathbb{L}_1\mathbb{L}_2)^{-1}\begin{pmatrix} \lambda_0 \\ \lambda_s \\ \lambda_c \end{pmatrix} + C_{aero}\right)$$

with $\lambda_s = \lambda_c = 0$ to account for the uniform inflow only. C_{aero}, $\mathbb{M}$, $\mathbb{L}_1$, $\mathbb{L}_2$ are reported in Ref. [10].

The expression of rotor-induced velocity at the disk, required in the calculation is:

$$v_i = (\frac{w_H}{\Omega R})\Omega R \tag{18}$$

Derivation of tip-path plane dynamic equation is detailed by Chen in Ref. [11].

Obtained equations are applied to counter-clockwise rotor by using the left-hand coordinate system and using a direction indicator χ in lateral equations, which value is equal to 1 when rotor is counter-clockwise; -1 otherwise, as in Ref. [12] and as presented by the authors in Ref. [7]. Resulting equations are given as follows:

$$\begin{aligned} \boldsymbol{V}_{cl} &= \Pi_1 \boldsymbol{V}_{ccl} \\ \boldsymbol{\Omega}_{cl} &= \Pi_2 \boldsymbol{\Omega}_{ccl} \\ \boldsymbol{F}_{cl} &= \Pi_1 \boldsymbol{F}_{ccl} \\ \boldsymbol{M}_{cl} &= \Pi_2 \boldsymbol{M}_{ccl} \\ \boldsymbol{U}_{cl} &= \Pi_1 \boldsymbol{U}_{ccl} \end{aligned} \tag{19}$$

provided $\Pi_1 = \begin{bmatrix} 1 & 0 & 0 \\ 0 & \chi & 0 \\ 0 & 0 & 1 \end{bmatrix}$, $\Pi_2 = \begin{bmatrix} \chi & 0 & 0 \\ 0 & 1 & 0 \\ 0 & 0 & \chi \end{bmatrix}$ and

$\boldsymbol{U} = [\theta_0 \quad A_{1s} \quad B_{1s}]$.

Rotors interference model

A generalized geometrical framework for addressing preliminary design of the two rotors is presented. Let d be the distance between the two main rotors hub on the rotorcraft buttline; h be the height over the rotor hub between the hub itself and the tip path plane of the other rotor. Let R be the rotor radius and R_{hub} be the hub length. Considering again Γ the angle between the rotors, referring to Figure 4:

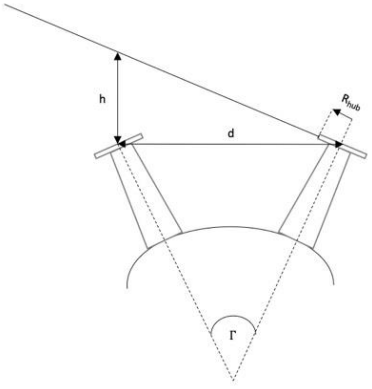

Figure 4: Synch-rotor geometry

If the distance between the rotors allows them not to collide, that is $d > R + R_{hub}$, Γ can be zero and the rotors masts can stay parallel. If $d \leq R + R_{hub}$, the masts should be tilted in order to avoid the collision, so the angle Γ should be different from zero. h states how much the rotors have to be tilted, it is a design parameter. Eq. (20) links d and Γ:

$$d = h \cot\frac{\Gamma}{2} \tag{20}$$

Figure 5 shows the trend of Γ in function of the normalized distance d/R for three different normalized values of h/R. For low angles Γ the distance is higher and for high angles the distance tends to zero.

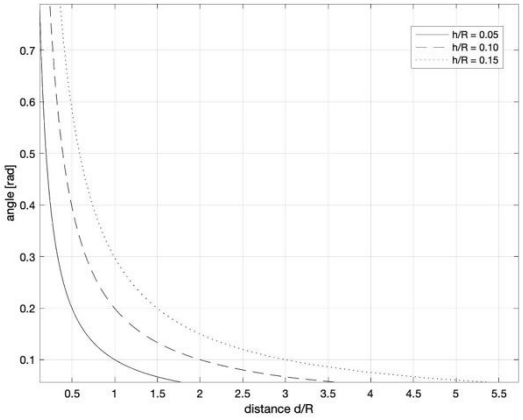

Figure 5: Trend of d vs Γ

Interference effects are included considering the overlapping between the two main rotors. These effects are consistent with those presented by Leishman in Ref. [13]. Since rotors are not coaxial, the rotor interference induced power factor k is adequately scaled in thrust computation, in order to account for the actual overlapping fraction of the disk area. k is the obtained multiplying the Leishman induced power factor for coaxial rotors by a scaling factor, that is the ratio between the overlapping area A_{ov} and the rotor area. Overlapping area between the rotors is calculated projecting the radius of a single tilted rotor from XY Hub-Body plane to the un-tilted XZ Body plane and considering the length of overlapping distance. The area is geometrically estimated, whereas seen from the top it appears as an intersection of two circular sectors. Then equivalent radius is estimated and the ratio between the areas is found, as depicted in Figure 6. Equations for overlapping area are as follows:

$$A_{ov} = 2 * A_{cs} - A_r \tag{21}$$

where $A_{cs} = \frac{{R_{pro}}^2 * \alpha}{2}$ is the area of the circular sector with projected radius $R_{pro} = R\cos\frac{\Gamma}{2}$ and angular opening $\alpha = 2\cos^{-1}(\frac{\mathrm{d}}{R_{pro}})$; $A_r = \mathrm{d} * R_{pro} * \sin\frac{\alpha}{2}$ is the area of the rhombus with diagonals d and $2R_{pro}\sin\frac{\alpha}{2}$.

Figure 5 shows the relationship between d/R,

Γ and the normalized overlapping area.

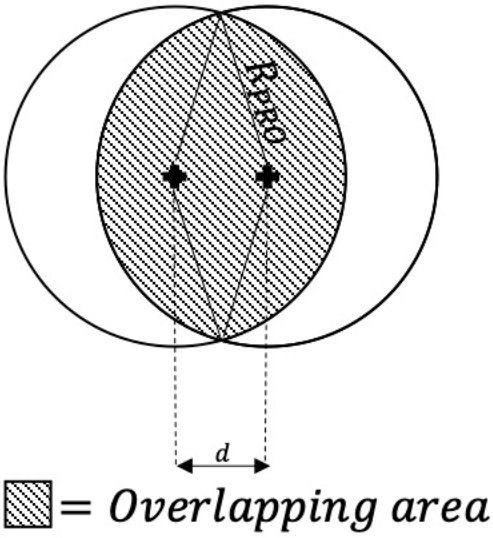

Figure 6: Overlapping area geometry

2.3.2 Airframe model

Fuselage and tail surfaces are modelled as follows.

The fuselage aerodynamic model provides forces and moments as a function of angle of attack and sideslip angle along the flight envelope. Effects are accounted into performance and stability analysis for forward speeds. Continuity in numerical estimation is mandatory in order to prevent unrealistic linear or angular accelerations in response to small changes in attitude. In this model, continuity is provided by a linear interpolation for forces and moments on angles range not covered. Details on the procedure and forces and moments equations are available in Ref [9].
Vertical fin and horizontal tail are considered as lift and drag producers and are approximated for all angles of attack and sideslip. Principal assumptions include:

1. Surfaces are modelled with symmetrical profiles;
2. An elliptical distribution with uniform downwash is considered;
3. Forces are applied at the quarter chord of each surface;
4. Maximum lift coefficient is specified;
5. Profile drag coefficient varies with angle of attack;
6. The induced drag coefficient at the square of the calculated lift coefficient.

Equations are given in detail by Talbot in Ref. [9].

3. LINEARIZED SYNCH-ROTOR EQUATIONS OF MOTION

Let $f(\dot{X}, X, U, t) = 0$ represent the non-linear model described by the classical Newton-Euler equations of motion projected in the body system:

(22) $$\dot{V} = -\Omega \times V + F^{(e)}/m$$

(23) $$\dot{\Omega} = I^{-1}\left[-\Omega \times (I\Omega) + M^{(e)}\right]$$

Let $X = \{u, w, q, \theta, v, p, \phi, r, \psi\}$ be the state vector and $U = \{A_1, \theta_0, B_1, \theta_{ped}\}$ be the control vector. With small perturbation theory, it can be assumed that during disturbed motion, the vehicle behaviour can be described as a perturbation from the equilibrium condition, written in the form:

(24) $$X = X_e + \delta X$$

where δX represents the perturbed state.

Taylor's theorem states that it is possible to estimate the behavior of an analytic function in its range if the function and all its derivatives are known at any one point (the so called trim condition). The function is expanded in a series about the known point. Fundamental assumptions of linearization are that external forces and moments can be expressed as analytic functions of the disturbed motion variables and their derivatives and that disturbances are assumed small. In this way, the dominant effect in the expansion results to be the linear one and higher order terms of Taylor's expansion are neglected. Aerodynamic forces and moments can be written in the form:

(25) $$\Delta F^{(a)} = \left[\sum_{n=1}^{N} X_{\lambda_i}\lambda_i \quad \sum_{n=1}^{N} Y_{\lambda_i}\lambda_i \quad \sum_{n=1}^{N} Z_{\lambda_i}\lambda_i\right]^T$$

(26) $$\Delta M^{(a)} = \left[\sum_{n=1}^{N} L_{\lambda_i}\lambda_i \quad \sum_{n=1}^{N} M_{\lambda_i}\lambda_i \quad \sum_{n=1}^{N} N_{\lambda_i}\lambda_i\right]^T$$

where $\lambda = \Lambda - \Lambda_0$, with Λ the vector of all variables affecting aerodynamic forces and moments, whose stability derivatives are written in a semi-normalized form with the notation:

(27) $$X_{\lambda_i} = \frac{1}{m}\frac{\partial X^{(a)}}{\partial \lambda_i}$$

for all forces, and

(28) $$M_{\lambda_i} = \frac{1}{I_{yy}}\frac{\partial M^{(a)}}{\partial \lambda_i}$$

for M moment stability derivatives, and, as examples,

(29) $$L'_p = \frac{I_{zz}}{I_{xx}I_{zz} - {I_{xz}}^2} L_p + \frac{I_{xz}}{I_{xx}I_{zz} - {I_{xz}}^2} N_p$$

(30) $$N'_r = \frac{I_{xz}}{I_{xx}I_{zz} - {I_{xz}}^2} L_r + \frac{I_{xx}}{I_{xx}I_{zz} - {I_{xz}}^2} N_r$$

for L and N ones.

Linearized equations in the state-space form are:

(31) $$\dot{X} = AX + BU$$

where the state and control matrices are obtained as:

(32) $$A = \left(\frac{\partial f}{\partial x}\right)_{x=x_e}$$
$$B = \left(\frac{\partial f}{\partial u}\right)_{x=x_e}$$

The state and the control matrices A and B have the same structure of those presented by Padfield [14] and are reported in appendix B, with the longitudinal and lateral decoupled state matrices A_{lon} and A_{lat}.

3.1. Stability derivatives

Aircraft stability derivatives are obtained both analytically, by using closed-form approximate models, and numerically, by applying central finite different method directly on simulation software [14]. On one hand, numerical linearization allows for a complete and accurate modelling of system dynamics. On the other hand, there may be a lack of physical understanding since relationship between aircraft design and dynamic behaviour is straightforward. In this respect, analytical approximations may help in addressing the dynamics analysis in a deeper detail. In what follows, according to Padfield approach [14], a selection of relevant stability derivatives of the synch-rotor configuration (see Table 0-1) are compared to numerical ones.

3.1.1 Translation velocity derivatives

Rotor flapping, changes in rotor lift and drag and the incidence and sideslip angles of the flow around fuselage and empennage are influenced by translational velocity perturbations. This gives rise to a complex behaviour, also considering that the orientation of the Body axes and the Hub ones are affected by the shaft tilt, rotor flapping and the sideslip angle. So, a u perturbation in Body axes causes μ_x, μ_y and μ_z perturbations in Hub axes.

Z_w

The aerodynamic force acting along z_B axes for a conventional helicopter configuration is [14]: $Z = -T_{MR}$where $T_{MR} = \rho A(\Omega R)^2 C_T$. For the synch-rotor configuration, Z results to be: $Z = -2T_{MR}\Pi_{hb}(3,3) = -2T_{MR}\cos\frac{\Gamma}{2}$. By differentiating with respect to z: $\frac{\partial Z}{\partial w} = -\frac{\partial\left(2\rho A(\Omega R)^2 C_T \cos\frac{\Gamma}{2}\right)}{\partial w} = -2\rho A(\Omega R)^2 \cos\frac{\Gamma}{2}\frac{\partial C_T}{\partial w}$.

Applying the chain rule for multi-variable functions the coefficient derivative is computed [7]:

(33) $$\frac{\partial C_T}{\partial w} = \left[\frac{\partial C_T}{\partial w_H}\frac{\partial w_H}{\partial w}\right] = \frac{1}{\Omega R}\left[\frac{\partial C_T}{\partial \mu_z}\Pi_{hb}(3,3)\right] = \frac{1}{\Omega R}\left[\frac{\partial C_T}{\partial \mu_z}\cos\frac{\Gamma}{2}\right]$$

where the derivative $\frac{\partial C_T}{\partial \mu_z}$ is provided by [14] for the hovering case:

(34) $$\frac{\partial C_T}{\partial \mu_z} = \frac{2a_0 s\lambda_0}{16\lambda_0 + a_0 s}$$

Z_w, known in literature as the heave damping derivative, is the initial acceleration following an abrupt vertical gust. It is highly influenced by the inverse of rotor blade loading $\frac{M_a}{A_b}$, which appears in equation (33) if it is normalized by M_a. This gives rise to a lower gust sensitivity with respect to fixed-wing aircrafts. In Table 3-1 values for Z_w calculated with the proposed analytical expression and numerically evaluated are reported with the percentage error in hovering and for $20\ km/h$. The semi-normalized form is used.

Table 3-1: Analytical vs numerical values for Z_w

Γ	$Z_w analytical$	$Z_w numerical$	$Error\ \%$
Hovering			
0°	-0.2535	*-0.2424*	*4.5701 %*
5°	*-0.2531*	*-0.2421*	*4.5212 %*
15°	*-0.2494*	*-0.2396*	*4.0747 %*
25°	*-0.2422*	*-0.2349*	*3.1077 %*
35°	*-0.2314*	*-0.2278*	*1.5637 %*
45°	*-0.2171*	*-0.2183*	*0.5477 %*
Airspeed 20 km/h			
0°	*-0.3594*	*-0.3778*	*5.1222 %*
5°	*-0.3575*	*-0.3771*	*5.4973 %*
15°	*-0.3500*	*-0.3714*	*6.1110 %*
25°	*-0.3383*	*-0.3601*	*6.4640 %*
35°	*-0.3230*	*-0.3437*	*6.4070 %*
45°	*-0.3051*	*-0.3225*	*5.7061 %*

Figure 7 shows Z_w and Z_u stability derivatives for different values of Γ along the flight envelope, considering straight-and-level flight at different airspeed at an altitude of $113\ m$. The dihedral angle does not have a strong influence on these stability derivatives and the trend is similar to that of a conventional single main rotor helicopter [14].

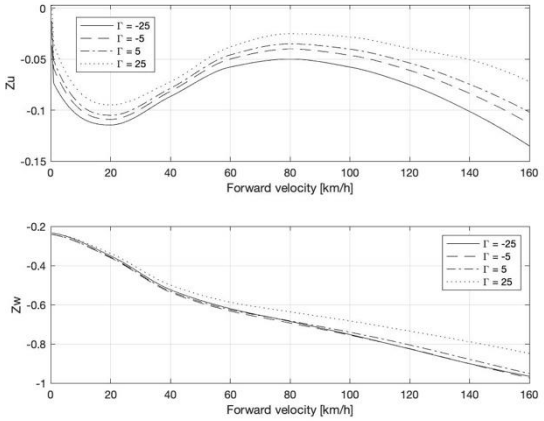

Figure 7: Stability derivatives – Z_w Z_u

X_u, X_v, Y_u, Y_v

The direct force dampings X_u *and* Y_v at high forward speed tend to be linear with velocity, like for conventional single main rotor helicopters [14], reflecting the drag and the sideforce. Discs tilts in response to u and v perturbations are the main reason of these direct derivatives. The coupling derivatives tends to zero. As for Z_w and Z_u, the dihedral angle does not influence strongly the derivatives trends, as in Figure 8 and Figure 9.

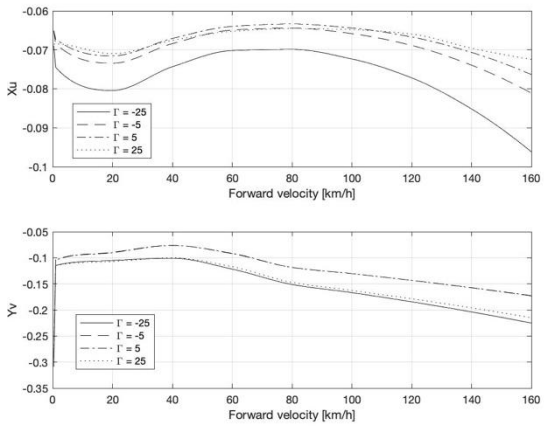

Figure 8: Stability derivatives – X_u Y_v

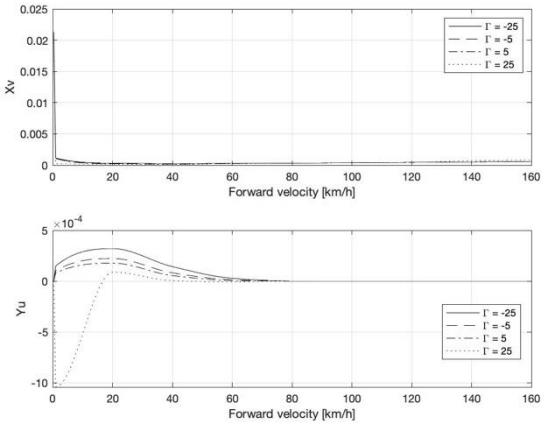

Figure 9: Stability derivatives – X_v Y_u

M_u, M_v, M_w

These stability derivatives are known as speed and static stability derivatives and have influence on handling qualities. Main rotor moments due to speed changes are almost constant, but aerodynamic moments from fuselage and horizontal and vertical tails notably vary with forward velocity. Especially for the horizontal stabilizer, whose normal load gives a pitching moment at the center of mass, affecting M_u. As for single main rotor helicopters, the static speed stability arises from the increase in forward speed that induced the disc to flap back and from an increment of the download on the horizontal stabilizer, bringing to a nose-up pitching moment that contributes to reduce the speed. As known from the literature [14], the incidence stability derivative M_w, as M_u, is given by the three contributions from main rotor, fuselage and horizontal stabilizer. In the case of a synchrotor helicopter, the contribution of the main rotor includes both the rotors. The horizontal stabilizer always contributes positively to M_w, in fact, to a positive change in w follows an increment in tailplane lift, resulting in a nose-down pitch moment. The contribution of a single main rotor is a combination of a moment proportional to the disc tilt and one to the thrust. It may be stabilizing or destabilizing, it depends on the position of the center of mass with respect to the thrust. If the center of mass is forward it is stabilizing. M_w results to be statically stable if it is negative. For both the derivatives, the dihedral angle does not give a strong contribution, as depicted in Figure 10.

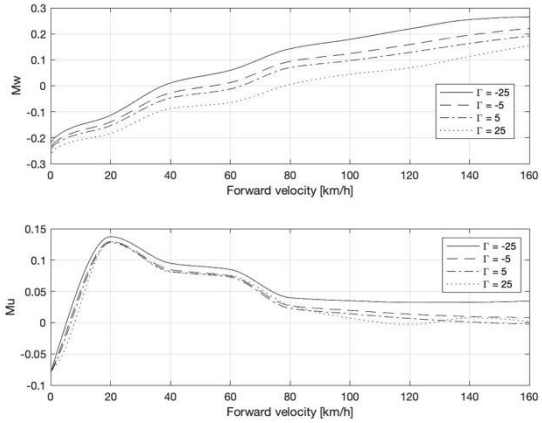

Figure 10: Stability derivatives – M_w M_u

L_u, L_v, L_w

The rolling moment derivatives are strongly related to the yawing ones, belonging to the lateral/directional stability derivatives. The so-called dihedral effect L_v is stabilizing if it is negative. As shown in Figure 11, a more negative value of L_v, that is more stabilizing, follows to a negative value of Γ, which corresponds to a positive value of the dihedral angle. With the increment of Γ from negative to positive values, gradually the dihedral effect tends to fewer negative values, indicating a less stabilizing effect. It is generated similarly to M_u. If a positive lateral velocity perturbation is applied to the synchrotor configuration, both rotors experience a rolling moment to port, even if the effect is greater for one and less for the other, due to the lateral shaft tilt. The rotor stiffness, the Lock number and the lift on the blades affect the amount of flap response.

L_u and L_w stability derivatives, together with N_u and N_w, influence the coupling of the longitudinal and lateral motions at low-frequencies. Figure 12 and Figure 13 show that increasing the forward velocity these derivatives tend to zero, as for a conventional single main rotor helicopter configuration [14]. The dihedral angle does not affect the behaviour.

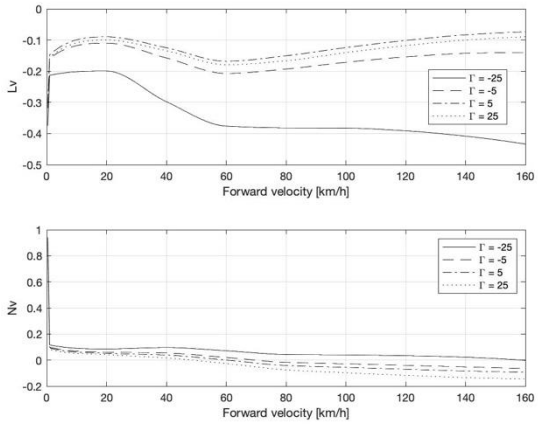

Figure 11: Stability derivatives – L_v N_v

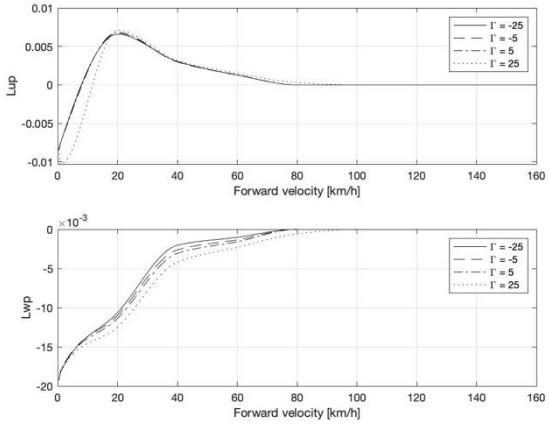

Figure 12: Stability derivatoves – L_u L_w

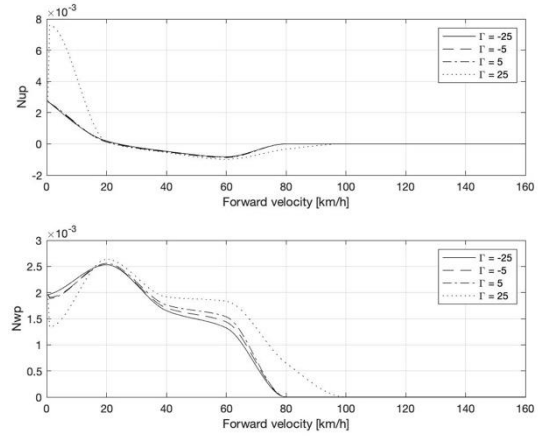

Figure 13: Stability derivatives – N_u N_w

$\mathbf{N_u, N_v, N_w}$

The weathercock stability derivative N_v for a single main rotor helicopter is given by the tail rotor, the fuselage and the vertical fin. In the case of synchrotor, only the fuselage and the vertical fin gives contribution to N_v. It is stabilizing with a positive value. The vertical fin contributes with a positive value; the fuselage is destabilizing if the pressure center is behind the center of mass. N_u and N_w arise from changes in rotors torque due to velocity perturbation, with the vertical fin giving its contribution to N_u similarly to horizontal stabilizer to M_u.

3.1.2 Angular velocity derivatives

The angular velocity force derivatives are often associated with the trim inertial velocity component, that, in some cases, have a primary effect and so the associated derivatives are negligible, like for example Z_q and Y_r.

$\mathbf{X_q, Y_p}$

X_q and Y_p are dominated by main rotors. The changes in X and Y forces bring a primary contribution to pitch and roll moments. If small drag forces are ignored, the rotor X force of the main rotor results to be $X = T\cos\frac{\Gamma}{2}a_1$. Accordingly, X_q depends by the flapping derivatives $\frac{\partial a_1}{\partial q}$, that is [15]: $\frac{\partial a_1}{\partial q} = -\frac{16}{\gamma\Omega}\left(1 - \frac{e}{R^2}\right)$.

This equation represents the disc lag following a pitch rate, that produces a pitch damping moment opposite to q. The Lock number γ, plays a crucial role. Y_p analysis agree with that resented above for X_q, with the only differences in sign and flapping angle. With respect to a conventional helicopter [14], the trend is opposite, due to the presence of two lateral tilted rotors.

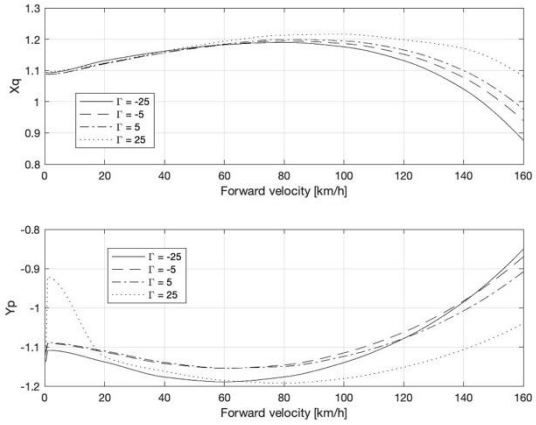

Figure 14: Stability derivatives – X_q Y_p

$\mathbf{M}_q, \boldsymbol{L_p}, \boldsymbol{M_p}, \boldsymbol{L_q}$

This set of stability derivatives has a fundamental role for dynamic analysis. M_q and L_p primary damping derivatives are related to handling characteristics and short-term, while the cross-coupling derivatives M_p and L_q are involved in the pitch-roll and roll-pitch couplings. These are mainly influenced by the main rotors. The moment due to in-plane rotor loads, the moment of the thrust vector tilt from the center of mass and the moment derived from the effective rotor stiffness are the principal components for both the rotor pitching and rolling moments. M_q stability derivative

has a strong influence at high speed by the horizontal tailplane [14].

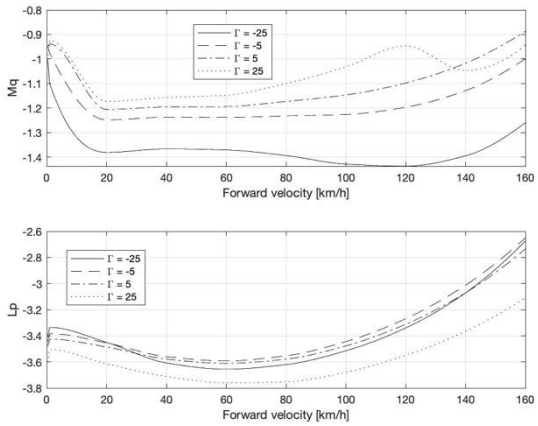

Figure 15: Stability derivatives – M_q L_p

Both M_q and L_p present a trend influenced by the presence of two tilted main rotors.

$\mathbf{N_r, L_r, N_p}$

These derivatives are involved in in lateral/directional stability and control characteristics of the aircraft. All the yaw derivatives are mostly influenced by the tail rotor and the vertical fin for a conventional single main rotor helicopter, especially the yaw damping derivative N_r. Considering the synchrotor configuration, the absence of the tail rotor contributes to lower the value of the yaw damping derivative.

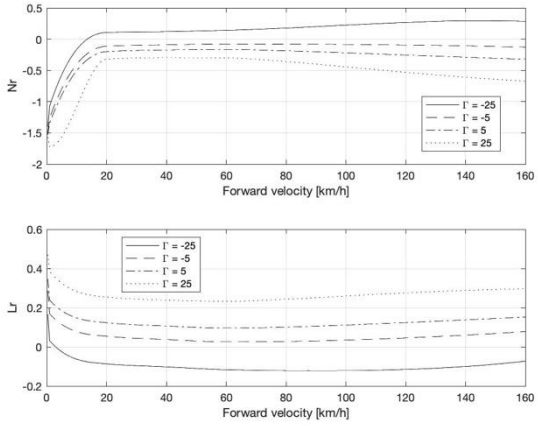

Figure 16: Stability derivatives – L_r N_r

The rolling moment due to yaw rate is mainly influenced by the vertical fin, since the tail rotor contribution is not present. The vertical tail sideforce increases to starboard as the aircraft nose goes to starboard, being L_r positive. L_r and N_r couple the roll and yaw together. Both are affected by the product of inertia I_{xz}, that couples the roll into the yaw. However, I_{xz} has powerful consequences on N_p stability derivative, that results to be more important [14].

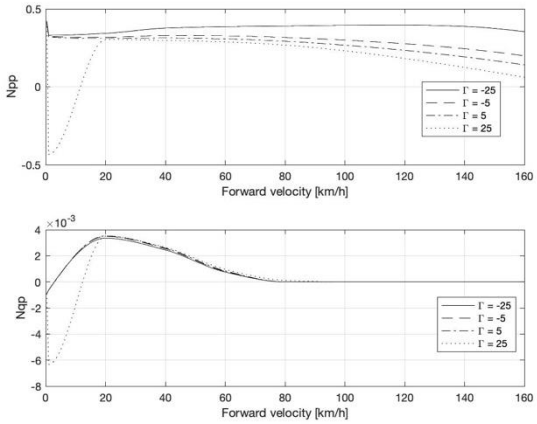

Figure 17: Stability derivatives – N_p N_q

4. STABILITY ANALYSIS

The linear model obtained in section 3 is used for stability analysis in both coupled and decoupled form. For this purpose, the equation associated to the heading angle state variable ψ is omitted, that is the kinematic equation relating the change of ψ euler angle to the rate p, q, r. The approximation done to decouple the system is that the eigenvalues fall into two separated sets on the complex plane, the longitudinal one and the lateral one. A numerical test case is discussed, based on the aircraft relevant parameters listed in Table 0-1.

Figure 18 illustrates the eigenvalues for the synch-rotor of the coupled system in hovering condition for Γ varying from $-45°$ to $45°$. Looking first to the phugoid mode, it is a stable oscillation for all the dihedral angles considered, differently from the Dutch-roll oscillation. In fact, for a negative value of the dihedral angle, this mode becomes unstable. The other modes are the stable roll subsidence and heave and the pitch-yaw coupled motion.

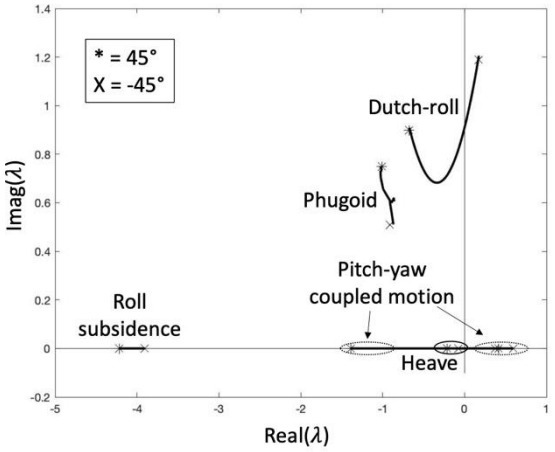

Figure 18: Loci of synch coupled eigenvalues as a function of different dihedral angle Γ in hovering

The principal difference between the coupled and uncoupled motions, reported in Figure 19 and Figure 20 lies in the stability of the Dutch-roll mode. This effect is

related to the strong contribution of the L_v stability derivative, that becomes more negative increasing the value of Γ.

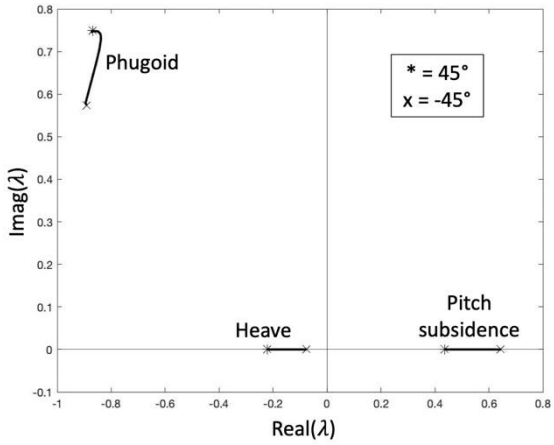

Figure 19: Loci of synch longitudinal eigenvalues as a function of the dihedral angle Γ in hovering

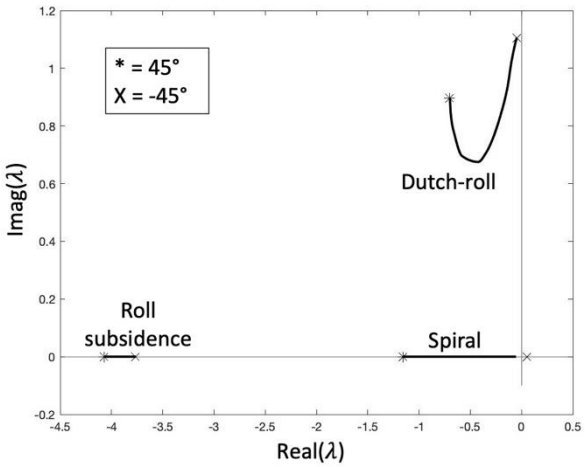

Figure 20: Loci of synch lateral eigenvalues as a function of the dihedral angle Γ in hovering

Figure 21, Figure 23 and Figure 22show the poles of the synch-rotor for both coupled and decoupled systems at a straight and level flight condition with a forward speed of $140\ km/h$ for different values of Γ. At high speed, the modes appear more coupled. The phugoid mode is no longer an oscillatory mode. Varying the dihedral angle from $-45°$ to $45°$, also the Dutch-roll becomes a non-oscillatory motion. The spiral motion, contrary to the hovering condition, is unstable. Figure 21, Figure 23 and Figure 22 are reported at the end of the paper for the sake of clarity.

4.1. Longitudinal dynamics

The longitudinal model involves the u, q, w and θ variables, in the form ported in appendix B.

At the hovering condition, for which is possible to reduce the order model, the approximation of the phugoid frequency and damping presented by Padfield [14] remain still valid for the synch-rotor configuration, that are:

$$\omega_p{}^2 \approx -g\frac{M_u}{M_q} \tag{35}$$

$$2\omega_p\zeta_p = -\left(X_u + g\frac{M_u}{M_q{}^2}\right) \tag{36}$$

Frequency and damping values for phugoid, together with the heave pole, are given in Table 4-1 for the synch-rotor configuration with a dihedral angle of $25°$:

Table 4-1: Comparison of exact and approximated values of phugoid frequency and damping and for the heave pole

Hovering	$\boldsymbol{\omega_p}$	$\boldsymbol{\zeta_p}$	$\boldsymbol{\frac{1}{T_h} = -Z_w}$
Exact	*0.353*	*0.3867*	*0.235*
Approximated	*-0.0834*	*-0.0863*	*0.244*
140 km/h	$\boldsymbol{\omega_p}$	$\boldsymbol{\zeta_p}$	$\boldsymbol{\frac{1}{T_h} = -Z_w}$
Exact	*0.0512*	*0.67*	*0.7903*
Approximated	*0.0328*	*2.2188*	*3.06*

At high forward speed, Padfield approximation for phugoid mode is not valid for the synch-rotor approximation, due to the strong coupling between the pitch and heave modes. The real pole associated to the vertical dynamic is given by $\frac{1}{T_h} = -Z_w$. The heave mode behaves as the phugoid one, being coupled at high forward velocity.

4.2. Lateral/directional dynamics

The lateral/directional model concerns the p, v, r and ϕ variables, rearranged in the form used by Padfield [14] and reported in appendix B. As for a conventional helicopter configuration, the involved modes are the Dutch-roll oscillation and the roll and spiral aperiodic subsidences. The roll subsidence mode is well characterized by the L_p stability derivative. For the synch-rotor, the roll damping stability derivative outlines the roll mode throughout the speed envelope. With regards to the spiral mode, the expression reported by Padfield is valid also for the synch-rotor for all the flight conditions. On the contrary, the approximation for the oscillatory Dutch-roll given in [14] is not suitable for the intermeshing configuration. In fact, this mode is no longer oscillatory at high speed, as depicted in Figure 23. Table 4-2 reports the exact and approximated values for the lateral/directional modes for the synch-rotor configuration with a dihedral angle of $25°$.

Table 4-2: Comparison of exact and approximated values of lateral/directional modes

Hovering	$\boldsymbol{\omega_d}$	$\boldsymbol{\zeta_d}$	$\boldsymbol{\lambda_r}$	$\boldsymbol{\lambda_s}$
Exact	*0.91*	*0.482*	*-4.07*	*-0.613*
Approx.	*0.6714*	*-4.1452*	*-3.6052*	*-0.4748*

140 km/h	λ_{d1}	λ_{d2}	λ_r	λ_s
Exact	*1.84*	*-2.62*	*0.0596*	*-3.44*
Approx.	ω_d	ζ_d	*0.0587*	*-3.3593*
	2.2467	*0.1728*		

The approximated expression for the spiral, roll and Dutch-roll mode employed are:

(37) $$\lambda_s \approx \frac{g}{L_p}\frac{(L_v N_r - N_v L_r)}{(U_e N_v + \sigma_s L_v)}$$

(38) $$\lambda_r \approx L_p$$

(39) $$2\omega_d\zeta_d \approx -\left(N_r + Y_v + \sigma_s\left\{\frac{L_r}{U_e} - \frac{L_v}{L_p}\right\}\right) / \left(1 - \frac{\sigma_s L_r}{L_p U_e}\right)$$

where $\sigma_s = \frac{g - N_p U_e}{L_p}$.

5. CONCLUSIONS

In this paper an analytical framework addressing the nonlinear and the linearized model is presented. Two decoupled subsystems and some approximate closed-form solutions for relevant dynamic modes are also derived together with a detailed stability analysis showing the relationship between aircraft configuration and dynamic behaviour is given, based on the presented linear model. Different design solutions, concerning the proper synch-rotor design parameters, that are the dihedral angle and the distance between the rotors, are investigated by a numerical test case and results in terms of stability derivatives and the related stability analysis are showed. In particular, stability analysis proved the strong influence of the dihedral angle with the lateral/directional dynamics, in particular for the Dutch-roll mode.

6. REFERENCES

[1] M. H. Mansur, M. B. Tischler, M. D. Bielefefield, J. W. Bacon, K. K. Cheung, M. G. Berrios and K. E. Rothman, "Full Flight envelope inner-loop control law development for the unmanned K-MAX," in *67th American Helicopter Society Annual Forum*, Virginia Beach, VA, May 3-5, 2011.

[2] C. R. Frost, M. B. Tischler, M. D. Bielefield and T. LaMontagne, "Design and test of flight control laws for the Kaman Burro unmanned aerial vehicle," in *AIAA, Atmospheric Flight Mechanics Conference*, Denver, CO, August 4-17, 2000.

[3] J. D. Colbourne, M. B. Tischler, C. A. Tomashofski and T. LaMontagne, "System identification and control system design for the Burro autonomous UAV," in *Proceedings for the American Helicopter Society 56th annual forum}*, Virginia Beach, VA, May, 2000.

[4] J. McGonagle, "The design, test and development challenges of converting the K-MAX helicopter to a heavy lift rotary wing UAV," in *Proceedings of the American Helicopter Society Annual Forum 57th*, Washington, DC, May 9-11, 2001.

[5] A. Barth, C. Spieb, K. Kondak and M. Hajek, "Design, Analysis and Flight Testing of a High Altitude Synchropter UAV," in *AHS International 74th Annual Forum&Technology Display*, Phoenix, Arizona, May 14-17, 2018.

[6] F. S. J. Wei, E. Moore and A. Gates, "An intermeshing rotor helicopter design and test," in *AIAA SciTech 2015*, Kissmmee, Florida, January 5-9, 2015.

[7] E. L. de Angelis, "Stability analysis of a multirotor vehicle hovering condition," *Aerospace science and technology,* no. 72, pp. 248-255, 2018.

[8] H. S. Choi, E. T. Kim, D. I. You and H. Shim, "Improvements in small-scale helicopter rotor modeling for the real-time simulation of hovering flight," *The Japan Society for Aeronautical and Space Sciences,* vol. 54, no. 185/186, pp. 229-37, 2011.

[9] P. D. Talbot, B. E. Tinling, W. A. Decker and R. T. N. Chen, "A mathematical model for a single main rotor helicopter for piloted simulation," Ames Reasearch Center, Moffett, Field, California, September 1982.

[10] D. A. Peters and N. HaQuang, "Dynamic inflow for pratical applications," *Journal of the American Helicopter Society,* vol. 33, no. 4, pp. 64-68, 1988.

[11] R. T. N. Chen, "A simplified rotor system mathematical model for piloted flight dynamics simulation," Ames Reaserach Center, NASA, Moffett Field, California, May 1979.

[12] H. S. Choi, E. T. Kim, D. I. You and H. Shim, "Improvements in Small-scale Helicopter Rotor Modeling for the Real-time Simulation of Hovering Flight," *The Japan Society for Aeronautical and Space Science,* vol. 54, no. 185/186, pp. 229-237, 2011.

[13] J. G. Leishman and M. Syal, "Figure of merit definition for coaxial rotors," *Journal of the American Helicopter Society,* vol. 53, no. 3, pp. 290-300, 2008.

[14] G. D. Padfield, Helicopter flight dynamics, Blackwell publishing, 1996.

[15] R. W. Prouty, Helicopter performance, stability and control, Krieger publishing company, Inc, 1989.

[16] G. Avanzini, E. L. de Angelis and F. Giulietti, "Optimal cruise performance of a conventional helicopter," *Journal of aerospace engineering,* vol. 0, no. 0, pp. 1-14, 2021.

APPENDIX A

Table 0-1: Relevant synch-rotor data

Parameter	Symbol	Value	Unit
Vehicle data			
Mass	m	794.4	kg
Principal moments of inertia	$I_x,\ I_y, I_z$	260.8476, 791.1295, 657.0265	kgm^2
Inertia products	$I_{xy},\ I_{yz}, I_{xz}$	0.4146, 0.0848, −65.9153	kgm^2
Stationline position of CG	STA_{CG}	2	m
Buttline position of CG	BL_{CG}	0	m
Waterline position of CG	WL_{CG}	1.2848	m
Rotor data			
Stationline position of hub	STA_H	*2*	m
Buttline position of left hub	BL_H	*0.25*	m
Buttline position of right hub	BL_H	*-0.25*	m
Waterline position of hub	WL_H	*2.4*	m
Number of rotor blades	N_{blades}	*2*	
Nominal angular velocity	Ω_{nom}	*396.3*	*RPM*
Radius	R	*2.8*	m
Mean chord blade	c	*0.195*	m
Flapping spring constant	K_β	*0*	*Nm/rad*
Pitch-flap coupling tangent	K_1	*0*	
Hinge offset	ϵ	*0*	m
Blade inertia moment	I_β	*27.3651*	kgm^2
Blade profile lift curve slope	Cl_α	*5.8101*	rad^{-1}
Blade twist angle	θ_{tw}	*-0.0742*	*rad*
Tip loss factor	B	*0.96*	
Precone angle	a_0	*0.0262*	*rad*
Solidity	σ	*0.0443*	
Lateral shaft tilt	Γ	*25*	*deg*
Fuselage			
Fuselage drag, $\boldsymbol{\alpha = \beta = 0}$	D_1	*0.2803*	m^2
Fuselage drag, variation with $\boldsymbol{\alpha}$	D_2	*-0.1377*	m^2/rad
Fuselage drag, variation with $\boldsymbol{\alpha^2}$	D_3	*1.307*	m^2/rad^2
Fuselage drag, variation with $\boldsymbol{\beta^2}$	D_4	*5.306*	m^2/rad^2
Fuselage drag, $\boldsymbol{\alpha = 90}$	D_5	*2.074*	m^2
Fuselage drag, $\boldsymbol{\beta = 90}$	D_6	*3.310*	m^2
Fuselage lift, $\boldsymbol{\alpha = \beta = 0}$	XL_0	*-0.08014*	m^2
Fuselage lift, variation with $\boldsymbol{\alpha}$	XL_1	*0.8635*	m^2/rad
Fuselage lift, variation with $\boldsymbol{\alpha^2}$	XL_2	*-1.256*	m^2/rad^2
Fuselage lift, variation with $\boldsymbol{\beta^2}$	XL_3	*-4.812*	m^2/rad^2
Fuselage lift, $\boldsymbol{\alpha = 90}$	XL_4	*1.359*	m^2
Fuselage lift, $\boldsymbol{\beta = 90}$	XL_5	*0.0136*	m^2
Fuselage side force, variation with $\boldsymbol{\beta}$	Y_1	*-2.062*	m^2/rad
Fuselage rolling moment, variation with $\boldsymbol{\beta}$	YL_1	*-1.956*	m^3/rad
Fuselage rolling moment, $\boldsymbol{\beta = 90}$	YL_2	*1.832*	m^3
Fuselage pitch moment, $\boldsymbol{\alpha = \beta = 0}$	XM_1	*-0.3069*	m^3
Fuselage pitch moment, variation with $\boldsymbol{\alpha}$	XM_2	*0.03538*	m^3/rad
Fuselage pitch moment, $\boldsymbol{\alpha = 90}$	XM_3	*-5.621*	m^3
Fuselage pitch moment, variation with $\boldsymbol{\alpha^2}$	XM_4	*4.038*	m^3/rad^2
Fuselage pitch moment, variation with $\boldsymbol{\beta}$	XM_5	*-0.1521*	m^3/rad
Fuselage pitch moment, variation with $\boldsymbol{\beta^2}$	XM_6	*18.57*	m^3/rad^2
Fuselage pitch moment, $\boldsymbol{\beta = 90}$	XM_7	*3.819*	m^3
Fuselage yawing moment, variation with $\boldsymbol{\beta}$	XN_1	*3.268*	m^3/rad
Fuselage yawing moment, $\boldsymbol{\beta = 90}$	XN_2	*7.79*	m^3
Fuselage yawing moment, $\boldsymbol{\alpha = 90}$	XN_3	*0.1527*	m^3
Horizontal stabilizer			
Stationline postion	STA_{HS}	*6.199*	m

Buttline postion	BL_{HS}	*0*	*m*
Waterline postion	WL_{HS}	*1.39*	*m*
Incidence angle	i_{HS}	*-2*	*deg*
Area	s_{HS}	*0.2145*	m^2
Aspect ratio	AR_{HS}	*4.71*	
Dynamic pressure ratio	η_{HS}	*0.633*	
Lift curve slope	Cl_{HS}	*1.1*	
Upper vertical fin			
Stationline postion	STA_{VF1}	*6.1*	*m*
Buttline postion	BL_{VF1}	*0*	*m*
Waterline postion	WL_{VF1}	*1.683*	*m*
Incidence angle	i_{VF1}	*-4*	*deg*
Area	s_{VF1}	*0.1544*	m^2
Aspect ratio	AR_{VF1}	*4.304*	
Dynamic pressure ratio	η_{VF1}	*0.41*	
Lift curve slope	Cl_{VF1}	*1.16*	
Sweep angle	λ_{VF1}	*33.16*	*rad*
Lower vertical fin			
Stationline postion	STA_{VF2}	*6.069*	*m*
Buttline postion	BL_{VF2}	*0*	*m*
Waterline postion	WL_{VF2}	*0.996*	*m*
Incidence angle	i_{VF2}	*-2*	*deg*
Area	s_{VF2}	*0.1268*	m^2
Aspect ratio	AR_{VF2}	*3.358*	
Dynamic pressure ratio	η_{VF2}	*0.54*	
Lift curve slope	Cl_{VF2}	*1.21*	
Sweep angle	λ_{VF2}	*33.15*	*rad*

$$\mathbf{B} = \begin{bmatrix} X_{\theta_0} & X_{\theta_{1s}} & X_{\theta_{1c}} & X_{\theta_{0T}} \\ Z_{\theta_0} & Z_{\theta_{1s}} & Z_{\theta_{1c}} & Z_{\theta_{0T}} \\ M_{\theta_0} & M_{\theta_{1s}} & M_{\theta_{1c}} & M_{\theta_{0T}} \\ 0 & 0 & 0 & 0 \\ Y_{\theta_0} & Y_{\theta_{1s}} & Y_{\theta_{1c}} & Y_{\theta_{0T}} \\ L'_{\theta_0} & L'_{\theta_{1s}} & L'_{\theta_{1c}} & L'_{\theta_{0T}} \\ 0 & 0 & 0 & 0 \\ N'_{\theta_0} & N'_{\theta_{1s}} & N'_{\theta_{1c}} & N'_{\theta_{0T}} \end{bmatrix}$$

$$A_{LON} = \begin{bmatrix} X_u & g\cos\Theta_e/U_e & X_w - g\cos\Theta_e/U_e & X_q - W_e \\ Z_u & g\sin\Theta_e/U_e & Z_w - g\sin\Theta_e/U_e & Z_q \\ Z_u & g\sin\Theta_e/U_e & Z_w - g\sin\Theta_e/U_e & Z_q + U_e \\ M_u & 0 & M_w & M_q \end{bmatrix}$$

$$A_{LAT} = \begin{bmatrix} 0 & 0 & Y_v & g \\ 0 & 0 & 1 & 0 \\ -N_r & -U_e N_v & N_r + Y_v & g - N_p U_e \\ L_r/U_e & L_v & -L_r/U_e & L_p \end{bmatrix}$$

APPENDIX B

State and control matrices A and B, and the decoupled ones A_{lon} and A_{lat} are here reported:

$$\mathbf{A} = \begin{bmatrix} X_u & X_w - Q_e & X_q - W_e & -g\cos\Theta_e & X_v + R_e & X_p & 0 & X_r + V_e \\ Z_u + Q_e & Z_w & Z_q + U_e & -g\cos\Phi_e\sin\Theta_e & Z_v - P_e & Z_p - V_e & -g\sin\Phi_e\cos\Theta_e & Z_r \\ M_u & M_w & M_q & 0 & M_v & \begin{matrix} M_p - 2P_e I_{xz})I_{yy} \\ -R_e(I_{xx} - I_{zz})I_{yy} \end{matrix} & 0 & \begin{matrix} M_r + 2R_e I_{xz} I_{yy} \\ -P_e(I_{xx} - I_{zz})I_{yy} \end{matrix} \\ 0 & 0 & \cos\Theta_e & 0 & 0 & 0 & -\Omega_a\cos\Theta_e & -\sin\Theta_e \\ Y_u - R_e & Y_w + P_e & Y_q & -g\sin\Phi_e\sin\Theta_e & Y_v & Y_p + W_e & g\cos\Phi_e\cos\Theta_e & Y_r - U_e \\ L'_u & L'_w & L'_q + k_1 P_e - k_2 R_e & 0 & L'_v & L'_p + k_1 Q_e & 0 & L'_r - k_2 Q_e \\ 0 & 0 & \sin\Phi_e\tan\Theta_e & \Omega_a\sec\Theta_e & 0 & 1 & 0 & \cos\Phi_e\tan\Theta_e \\ N'_u & N'_w & N'_q - k_1 R_e - k_3 P_e & 0 & N'_v & N'_p - k_3 Q_e & 0 & N'_r - k_1 Q_e \end{bmatrix}$$

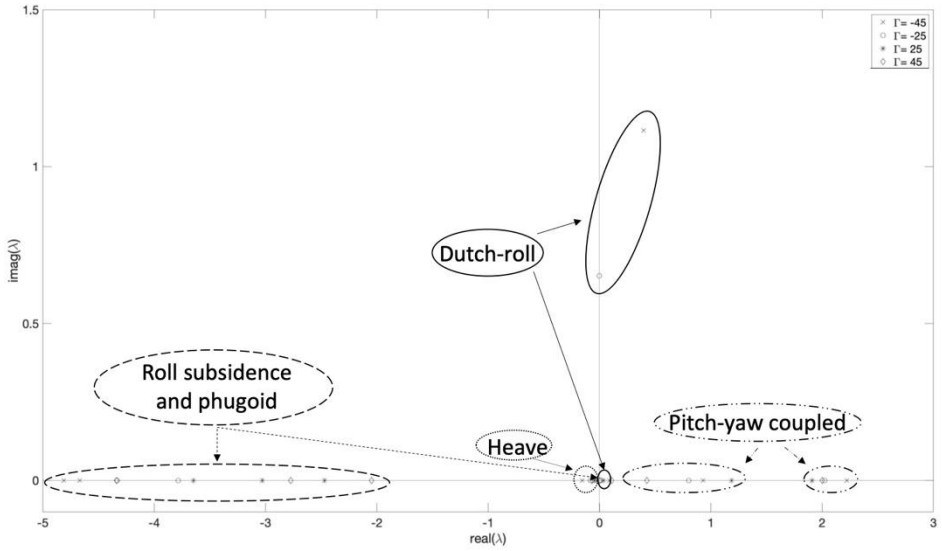

Figure 22: Loci of synch coupled eigenvalues as a function of different dihedral angle Γ at 140 km/h

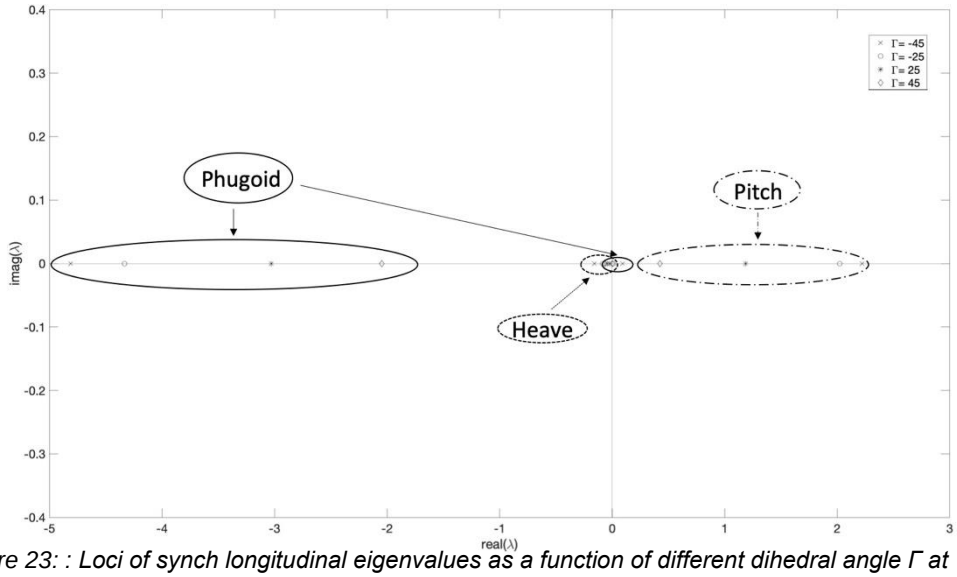

Figure 23: : Loci of synch longitudinal eigenvalues as a function of different dihedral angle Γ at 140 km/h

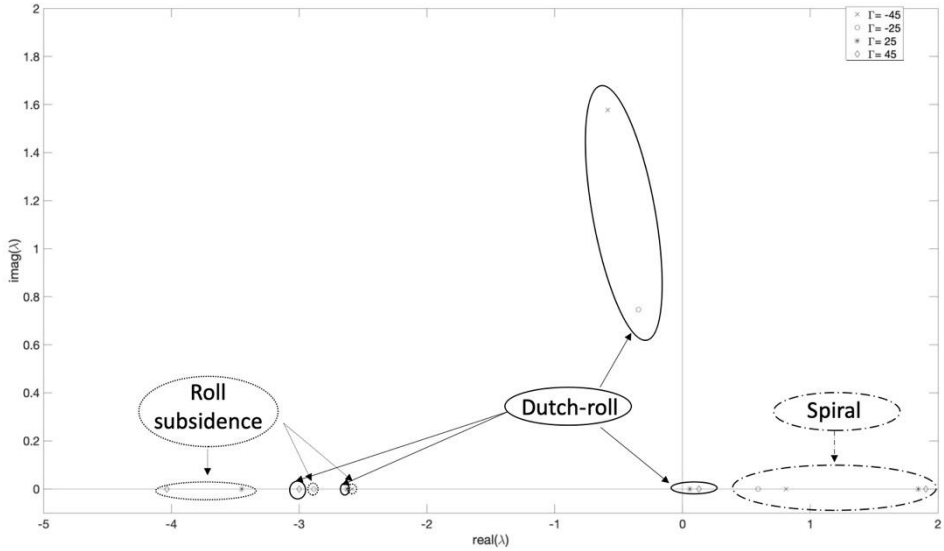

Figure 21: Loci of synch lateral eigenvalues as a function of different dihedral angle Γ at 140 km/h